Rotordynamic Force Prediction of Whirling Centrifugal Impeller Shroud Passages Using Computational Fluid Dynamic Techniques

J. J. Moore

A. B. Palazzolo

Department of Mechanical Engineering,
Texas A&M University,
College Station, TX 77843-3123

The demand for higher efficiencies and performance of modern centrifugal turbomachinery requires improved knowledge of critical design factors in strength of materials, aerodynamics, and rotordynamics. While tremendous strides in finite element stress analysis and computational fluid dynamics (CFD) have addressed the first two areas, the lack of accurate prediction tools for centrifugal impellers typically leaves rotordynamics out of the design loop. While several authors have analyzed the rotordynamic forces arising from shrouded centrifugal impellers, there has been no study to couple the secondary shroud passage with the three-dimensional primary flow model. The strong interaction between these domains makes this approach advantageous. The current study utilizes CFD techniques to analyze the full three-dimensional viscous, primary/secondary flow field in a centrifugal pump impeller to determine rotordynamic forces. Multiple quasi-steady solutions of an eccentric three-dimensional model at different precessional frequency ratios yield the rotordynamic impedance forces. Performing a second-order least-squares analysis generates the skew-symmetric stiffness, damping, and mass matrices. The results show good correlation with experiment for both performance and rotordynamic forces. [DOI: 10.1115/1.1385829]

Introduction

Fluid dynamic forces play a significant role in many turbomachines including single and multistage centrifugal compressors and pumps. The trend for more efficient designs with higher power densities have made an even greater challenge to the modern rotordynamicist. Much of the effort have focused on bearings and seals providing good design tools for these components. Centrifugal impellers typically play a strong role in the resulting stability of multi-stage machines. However, the source and mechanism of these destabilizing forces are probably the least understood. Many designers are forced to rely on empirically based guidelines such as those provided by Wachel et al. [1] Bolleter et al. [2], and Jery et al. [3]. The goal of this study is to improve the prediction of rotordynamic forces arising from the secondary flow passage of shrouded centrifugal impellers using modern CFD techniques.

Review of Experimental Data. Jery et al. [3] investigated the impedance forces from a three-dimensional centrifugal pump impeller ($R_2 = 16.2$ cm, $\beta 2 = -65$ deg, five blades, $N_s = 0.57$) over a range of precessional frequency ratios from -1.0 to 1.0. A trapezoidal volute with no diffuser was utilized. The resulting curves match a parabolic shape, yielding negative direct stiffness (K) and positive cross-coupled stiffness (k). The shroud clearance in this data is unrealistically high compared to most turbopump designs and underestimates the rotordynamic contribution from the shroud. Adkins and Brennen [4] indicate that shroud accounts for 80 percent of the direct stiffness of the entire impeller force and 33 percent of the cross-coupled stiffness; however, these percentages will be higher for typical shroud clearances. Clearances of 2.5 to 9.0 mm are observed in four modern rocket engine turbopumps including the space shuttle main engines (SSME) ([5]).

Ohashi et al. [6] presented additional data for a two-dimensional and three-dimensional impeller ($R_2 = 33$ and 35 cm, $\beta_2 = -68$, and -66 deg, six blades, respectively) in a vaneless diffuser and a three-dimensional impeller with vaned diffuser. Both the two-dimensional and three-dimensional data with vaneless diffuser showed essentially no destabilizing force (k) at the design flow. The results of the three-dimensional impeller (w/large shroud clearance) showed that the fluid forces with the vaned diffuser is about 50 percent greater than with a vaneless diffuser but still resulted in zero cross-coupled stiffness. The effect of shroud clearance was investigated by adding a spacer yielding a 2.7–3.0 mm shroud clearance. The tighter clearance raised the precessional frequency ratio at the stability threshold (WFR) from 0 to about 0.5. According to this data, the shroud is the dominant source of direct and cross-coupled stiffness for impellers with typical shroud clearances.

Bolleter et al. [7] utilized an impeller test rig based on a horizontal "rocking-arm" principle to test a 13.8 in. (350 mm) boiler feed pump impeller ($n_q = 33$) with vaned diffusers. In order to eliminate the effect of the wear-ring seal, a face seal was employed. These authors [2] went on to test three additional impeller configurations and investigate the effect of impeller to shroud wall clearance at entrance (so called "Gap A") and the impeller to diffuser vane clearance ("Gap B"). At the same speed with design flow, Bolleter et al. [7] shows three times the cross-coupled stiffness (nondimensional) compared to the data of Jery et al. [3] clearly due to the smaller shroud clearance. The data of Bolleter et al. [7] is utilized in the present study since it represents a more common impeller geometry and is accompanied with detailed performance measurements.

Guinzburg [8] presents results for a simulated shroud only pas-

Contributed by the International Gas Turbine Institute (IGTI) of THE AMERICAN SOCIETY OF MECHANICAL ENGINEERS for publication in the ASME JOURNAL OF ENGINEERING FOR GAS TURBINES AND POWER. Paper presented at the International Gas Turbine and Aeroengine Congress and Exhibition, Indianapolis, IN, June 7–10, 1999; ASME Paper 99-GT-334. Manuscript received by IGTI, October 1998; final revision received by the ASME Headquarters, March 1999. Associate Editor: D. Wisler.

sage using an external pump loop and tests for varying precessional frequency ratios, shroud and exit seal clearances, whirl radii, leakage flow rates, and speeds. Sivo et al. [9] continues this work by investigating the effect of meridional swirl brakes installed in the test section. Uy [5] makes similar measurements for a curved shroud passage.

Review of Theoretical Studies. Many authors have focused on the impeller/diffuser interaction including Colding-Jørgensen [10] using two-dimensional potential flow theory, Adkins et al. [4] using a quasi one dimensional model including unsteadiness, and Fongang et al. [11] with an improved potential flow model. A recent study utilizing an unsteady two-dimensional CFD calculation was performed by Torbergsen and White [12] and makes fluid dynamic comparisons to previously published data. While rotordynamic impedance forces were calculated, no comparison is made to experiment.

Other authors have studied the rotordynamic forces arising from only the shroud passage. Childs [13] expanded his incompressible, turbulent, concentric bulk flow seal model for constant radius to a variable radius model by casting the axial momentum in the pathwise, meridional direction. The resulting radial impedance curves generated by the bulk flow analysis showed substantial ''resonances'' for inlet swirls exceeding 0.5. The resonant peaks are attributed to the centrifugal acceleration term in the path momentum equations. Comparisons are made to the results of Bolleter [7] as will be shown later.

Contrary to the assumptions built into the bulk-flow theory, the shroud region typically contains many recirculation zones. Several authors have utilized the capabilities of computational fluid dynamics (CFD) to model the shroud region. Baskharone, Daniel, and Hensel [14] also modeled the isolated impeller shroud region for the Sulzer impeller (with face seal). Using a three-dimensional model, the discretized finite element flow governing equations are perturbed algebraically using a virtual eccentricity. A single-block grid was utilized that only includes only a portion of the primary flow path (up and down stream of the impeller) and results in a grid with high skewness requiring radiused corners. These results will also be compared with the present study Wyman [15] eliminates the need to prescribe boundary conditions leading into the shroud region by including the primary flow path in the model. However, only a two-dimensional model is developed and no rotordynamic coefficients are presented.

Several other authors have utilized CFD for modeling annular seals including Dietzen and Nordman [16], Rhode, Hensel, and Guidry [17] and Arghir and Frêne [18]. All of these authors employ a coordinate transformation from the three-dimensional eccentric domain into a two-dimensional axisymmetric one. These techniques require a zeroth-order solution and first-order calculations at the different precessional frequency ratios. The procedure is efficient but the coordinate transformation is only valid for constant radius seal geometries preventing the modeling of impeller shrouds. The CFD code SCISEAL, developed by Athavale et al. [19], utilizes a three-dimensional whirling method and solves for the quasi-steady flow field in an eccentric three-dimensional annular passage. This approach is more computationally intensive but is more general in the class of problems that may be solved. Moore and Palazzolo [20] use this code to make comparison to three-dimensional laser Doppler anemometer and rotordynamic measurements for grooved liquid annular seals. Their results show the κ-ε turbulence model with wall functions yielding close prediction of mean velocity profiles and reasonable calculation of rotordynamic force coefficients.

The present study utilizes a similar three-dimensional whirling method to analyze a three-dimensional eccentric shroud model that is coupled to the primary impeller flow. Being a steady solution, significantly less CPU time is required compared to unsteady approaches. Potentially the results of an impeller/diffuser interaction model could be added to the current shroud model to obtain the total force acting on the impeller.

Computational Fluid Dynamics Code Description

This study utilizes the commercial CFD code TASCflow from AEA [21]. The Reynolds-averaged Navier-Stokes equations (shown in Eq. (1) using index notation) are solved in strong-conservative form utilizing an algebraic multigrid solver and is applicable to both incompressible and compressible flows. The code allows solutions for both rotating and stationary frames of reference, using body-fitted structured grids of multidomains.

$$U_j \frac{\partial U_i}{\partial x_j} = \frac{1}{\rho} \frac{\partial}{\partial x_j} (-P\delta_{ij} + 2\mu S_{ij} - \overline{\rho u_i u_j}) \tag{1}$$

Both compressible and incompressible flow fields may be modeled using the standard κ-ε turbulence model. The turbulent Reynolds stresses are approximated using the Boussinesq eddy viscosity principle given in Eq. (2).

$$-\rho \overline{u_i u_j} = \mu_t \left(\frac{\partial U_i}{\partial x_j} + \frac{\partial U_j}{\partial x_i} \right) - \frac{2}{3} \rho \kappa \delta_{ij} \tag{2}$$

The turbulent, or eddy, viscosity is related to the turbulent kinetic energy (κ) and the dissipation rate (ε) by

$$\mu_t = \rho C_\mu \frac{\kappa^2}{\varepsilon} \tag{3}$$

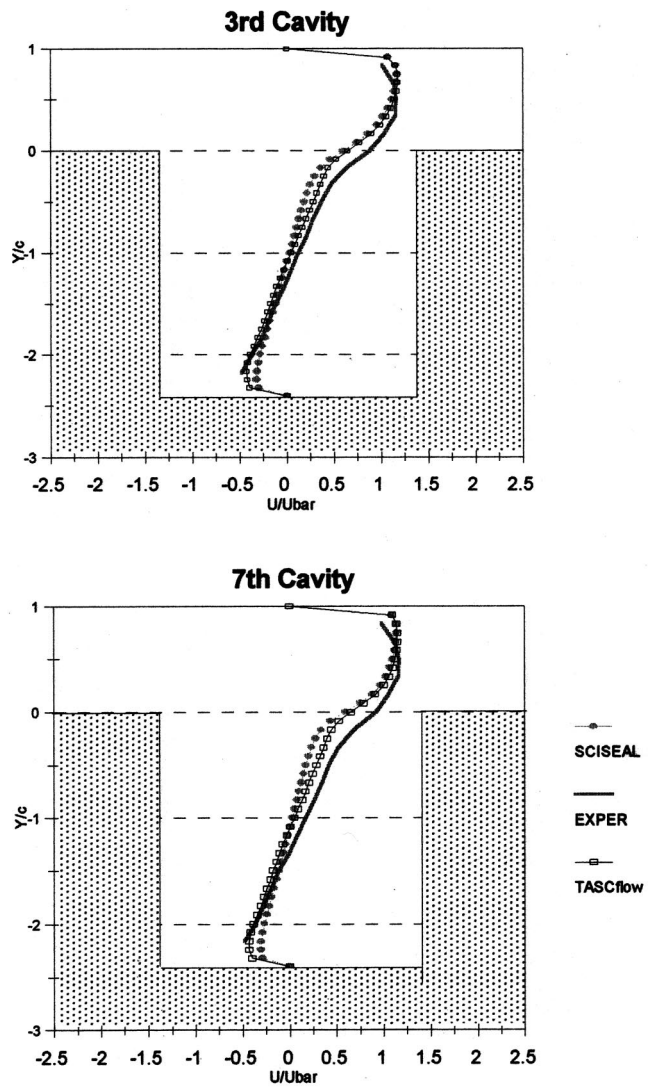

Fig. 1 Axial velocity profiles, grooved liquid annular seal

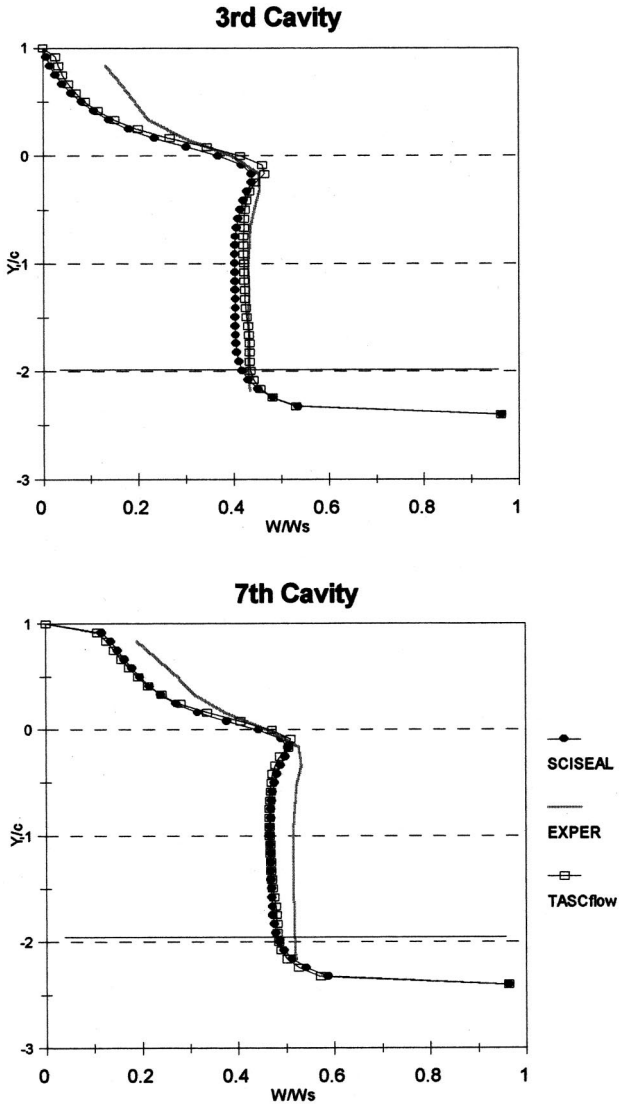

Fig. 2 Circumferential velocity profiles, grooved liquid annular seal

where the turbulent kinetic energy is defined as

$$\kappa = \frac{1}{2}\overline{u_k u_k}. \tag{4}$$

The law of the wall formulations models the sharp velocity gradients near the wall

$$u^+ = y^+ \quad \text{for } y^+ < 11.5 \tag{5}$$

$$u^+ = \frac{U_\tau}{K}\ln(Ey^+) \quad \text{for } y^+ > 11.5 \tag{6}$$

where

$$y^+ = \frac{yU_\tau}{\nu}, \quad u^+ = \frac{u}{U_\tau} \tag{7}$$

and

$$U_\tau = \sqrt{\frac{\tau_w}{\rho}}. \tag{8}$$

In order to obtain accurate wall shear stress, care is taken to ensure the near-wall grid points are placed in the logarithmic region (ideally $20 \leqslant y^+ \leqslant 200$). A full description of the theoretical aspects of the code may be obtained from AEA [21]. Raw [22] provides a complete description of the multi-grid solver.

CFD Comparison to three-dimensional LDA Measurements In order to validate the code for annular flows, comparisons are made to the three-dimensional laser Doppler anemometer (LDA) measurements of Morrison et al. [23] for a grooved liquid annular seal. This flow field is Couette in nature (due to the spinning journal) and contains regions of strong recirculation and high turbulence intensity. The seal tested is an eight-tooth, teeth-on-rotor design (radius = 82.05 mm, clearance = 1.27 mm, tooth width = 1.524 mm, and cavity = 3.048 mm square) spinning at 3600 rpm with a leakage rate of 4.86 1/s. The grid used is identical to that used by Moore and Palazzolo [20] who verified grid independence, allowing direct comparison to both experiment and SCISEAL predictions.

Figure 1 compares the axial velocity profiles at a section in the middle of the third and seventh seal cavities. The ordinate represents the radial position (Y) nondimensionalized with the clearance (cl), while the abscissa is the axial velocity nondimensionalized by the mean velocity in the through-flow jet (Ubar = 7.4 m/s). The through-flow jet, shear layer, and recirculation zones are clearly evident in this plot. The CFD computation predicts a steeper boundary layer near that stator (top) wall but yields essentially identical peak velocities as the experiment. TASCflow shows slight improvement over SCISEAL in capturing the strength of the recirculation in the cavity. Figure 2 shows similar plots at the same sections but for circumferential (swirl) velocity. Accurate prediction of swirl velocity is crucial to successful rotordynamic prediction. In the third cavity, both codes demonstrate good swirl prediction for both magnitude and distribution, with TASCflow showing slightly better agreement. By the seventh cavity, both codes slightly under predict the measured swirl. This study demonstrates that good mean flow prediction is possible using the standard κ-ε turbulence model with wall functions, even for swirling annular flows with strong recirculations.

Rotordynamic Solution Technique

A software interface to the TASCflow code is developed to generate the perturbed mesh and post process the results, yielding rotordynamic information. A full three-dimensional combined primary/secondary flow model is built using a multiblock body-fitted mesh and solved by performing a multiple frame of reference (MFR) solution, where a different frame of reference is used in different parts of the domain. A sliding interface is required at the boundaries between these domains.

The whirling, unsteady problem is transformed into a steady one by solving the three-dimensional eccentric flow field in the frame of reference attached to the whirling rotor (Fig. 3). In this rotating frame, the stator wall moves in the opposite direction (for positive whirl). The rotor surface moves with, against, or not at all relative to the whirling frame of reference, depending on the precessional frequency ratio (PFR) defined as the ratio of rotor whirl to rotor spin. Quasi-steady solutions are obtained at each PFR. A PFR equal to unity is termed synchronous whirl, where the shroud is whirling at the same frequency it rotates. A PFR of zero indicates a static displacement of the shroud, which then simply spins.

The choice of eccentricity is arbitrary but is typically kept near 10 percent of the shroud clearance to capture the linear, small motion characteristics. This value was arrived at based on previous modeling of annular seals ([20]). Larger eccentricities are possible and may be utilized to predict non-linear characteristics. The eccentricity vector is along the Y-axis.

A solution is obtained at multiple PFR values typically ranging from 0.0 to 2.0. The Cartesian area components of each cell face in the grid are stored. The X and Y area components on the (outer) surface of the shroud are multiplied by the local static pressure then summed for all cells on the shroud surface yielding F_l and F_n, respectively, as shown in Eqs. (9) and (10).

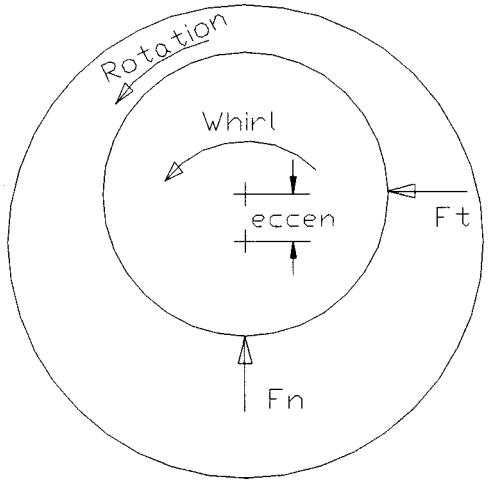

Fig. 3 Schematic of whirling rotor

$$F_n = \sum_{\text{shroud}} PA_y \tag{9}$$

and

$$F_t = \sum_{\text{shroud}} PA_x \tag{10}$$

A similar procedure is performed on all surfaces of the primary impeller passage (including blades) resulting in impedances for the impeller, showing the effect from shroud circumferential pressure distributions. The shear stress contribution at the wall contributes less than 1 percent of the total impedance force and is ignored. These impedance forces may be normalized by ϵ yielding the impedance both normal and tangential to the whirl orbit. A comparison of these impedance forces to a linear, second-order model is shown in Eqs. (11) and (12).

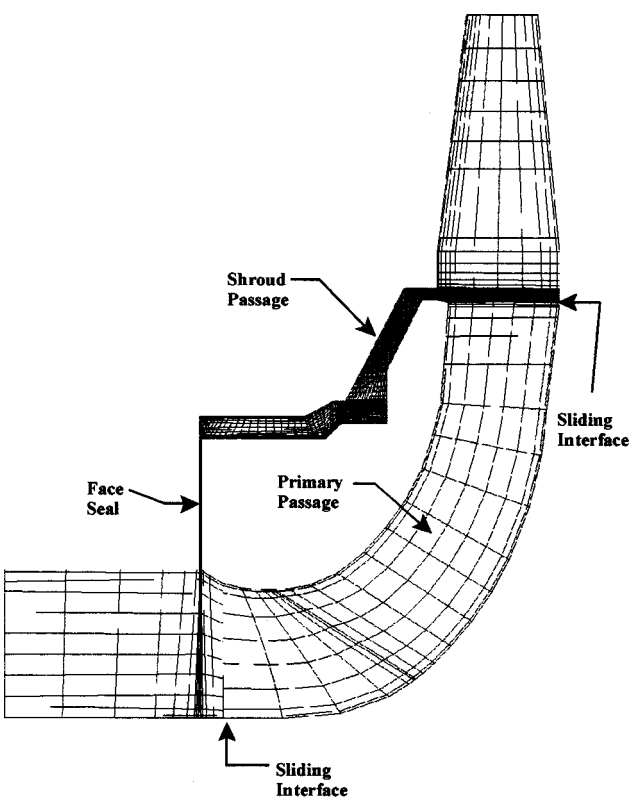

Fig. 4 Meridonial plane of combined primary/secondary model

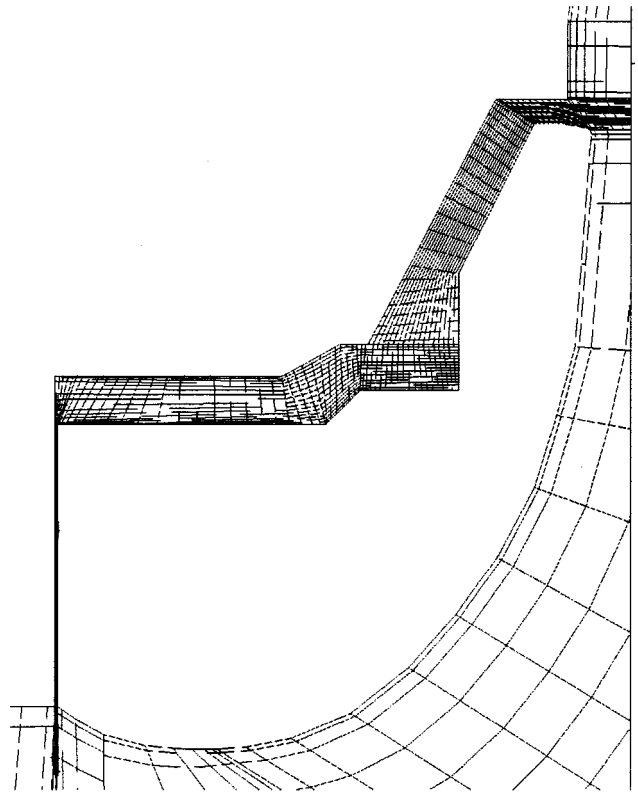

Fig. 5 Mesh of shroud region

$$\overline{F}_a = \frac{F_a}{\epsilon} = -K - c\Omega + M\Omega^2 \tag{11}$$

$$\overline{F}_t = \frac{F_t}{\epsilon} = k - C\Omega - m\Omega^2 \tag{12}$$

Each of the above equations represent one equation and three unknowns. The force coefficients are evaluated by determining the impedance force at multiple precessional frequencies (Ω). A minimum of three is required. For improved accuracy over a wide range of precessional frequencies, more than three are calculated (seven for this study), and a curve-fit to the linear second-order model is performed. The coefficients of the curve-fit yield the impeller's stiffness, damping, and mass force coefficients (K,k,C,c,M,m). The generality of this approach allows modeling of all variety of geometries including both seals and impeller shrouds.

Since the shroud region is solved in the whirling frame of reference (Ω) while the primary impeller passage is always solved in the rotating frame (ω), a sliding interface is employed. There are several possible locations of the sliding interface, but the best results were achieved placing the sliding interface across the primary flow just up and downstream of the impeller (see Fig. 4). Therefore, the inlet region leading into the impeller, face seal, shroud region, and diffuser section are all solved in the whirling frame of reference. The bladed impeller region is always solved in the rotating frame of reference (synchronous with impeller rotation).

The shroud region is made up of two grid blocks to minimize grid skewness and optimize node placement as shown in Fig. 5. The face seal, inlet region, and diffuser section each contain a separate grid block all connected using a structured interface. Since only shroud forces are of interest in this study, only the

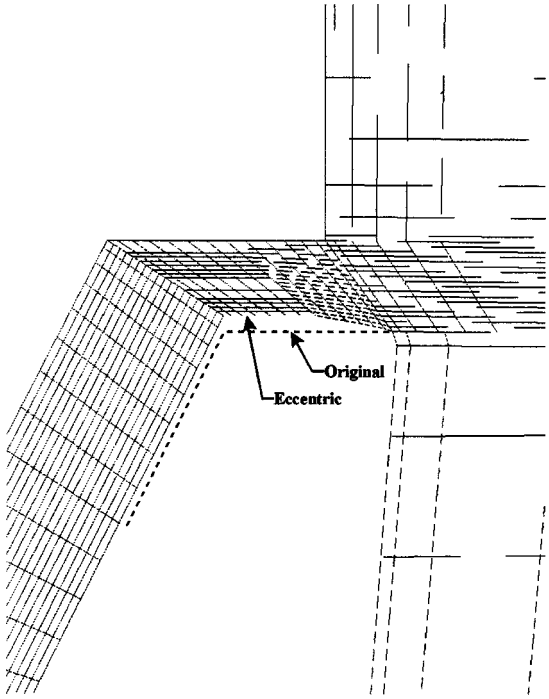

Fig. 6 Interface with impeller exit showing eccentric shroud

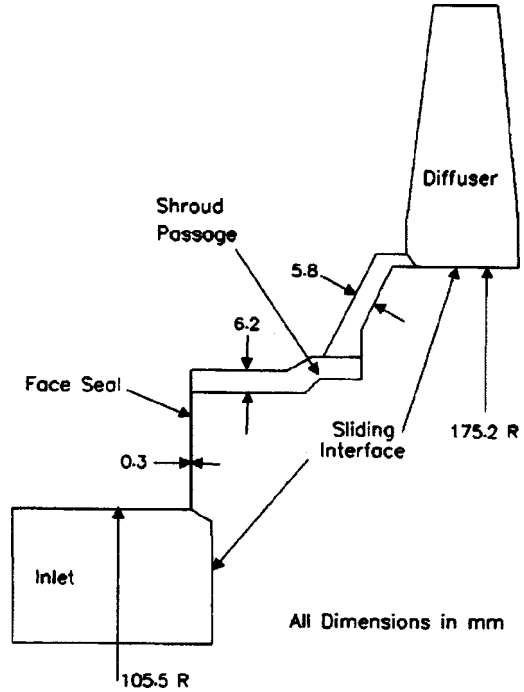

Fig. 7 Layout of shroud model

shroud region is made eccentric (see Fig. 6). As assumed by previous authors, the diffuser vanes are ignored in this model. The diffuser width is adjusted to mimic the actual flow area in the diffuser.

Boundary Conditions. Total pressure is specified at the inlet while velocity is specified (in absolute coordinates) at the diffuser exit and is done to ensure a circumferentially uniform flow field. The values are specified in cylindrical coordinates based on averaged velocities obtained from the centered case ($\epsilon=0$) using a mass flow boundary condition. Any nonuniformities in the model besides the eccentric shroud will yield false radial forces and affect the rotordynamic force prediction. Smooth, no-slip boundary conditions are assumed at all walls using wall functions.

TASCflow offers two sliding interface options: stage and frozen rotor. Stage performs circumferential averaging of the flow quantities, while frozen rotor performs a local transformation at each interface node. Strict conservation of all flow properties is maintained with both methods. The frozen rotor approach was chosen for both sliding interfaces so as to not artificially constrain the circumferential pressure field and is used exclusively in this study. This sliding interface does not require one-to-one matching of nodal points simplifying grid construction.

The spinning wall in the shroud region requires special treatment. It's relative rotation velocity (as observed in the whirling frame of reference) is a function of the precessional speed:

$$\omega_{\text{shroud}}=\omega-\Omega. \tag{13}$$

Its rotation vector is displaced by the eccentricity vector and is (0,0.6e-3,−1), since an eccentricity (ϵ) of 0.6 mm in the *Y*-direction is used for this study and impeller rotation is about the -*Z*-axis.

Eccentric Grid Generation. Accurate rotordynamic prediction requires a quality eccentric grid. First, a two-dimensional axisymmetric mesh in the meridonal (*R-Z*) plane is created as shown in Fig. 7. Nodes are distributed in the body fitted mesh to adequately resolve the important flow details. Care is taken in placement of the near wall nodes so as to not violate wall function criteria ($y^+>11.5$). This two-dimensional grid is saved in a PLOT3D format and read by a FORTRAN code. The grid is made eccentric by a specified value using control points in the grid coordinate directions (*i* and *j*). Only the three grid blocks representing the shroud are made eccentric. Appropriate transition regions are required near the impeller tip (Fig. 6). For more detail on the grid eccentricity algorithm, see Bhattacharya [24].

The impeller model is created with Turbogrid ([21]) using geometry information obtained from Sulzer Brothers, Ltd. The edge of the grid is centered between the impeller blades and represents an exact periodic section (360 deg/seven blades). Six additional grids are created from this grid by rotation about the spin axis (-Z) to create a full 360 deg impeller model (Fig. 8). The impeller blades are created by "blocking out" cells in those regions. Although appearing coarse, this particular grid is the result of a grid density study using a single impeller passage, where the predicted head rise is compared to measurements. A coarse, medium, and finer shroud grid is utilized in this study with identical impeller grids and is summarized in Table 1.

Note that the *I,J,K* local coordinate directions for the impeller are pathwise (*I*), circumferential (*J*), and cross-path (*K*), while all other blocks are pathwise, cross-path, and circumferential. All

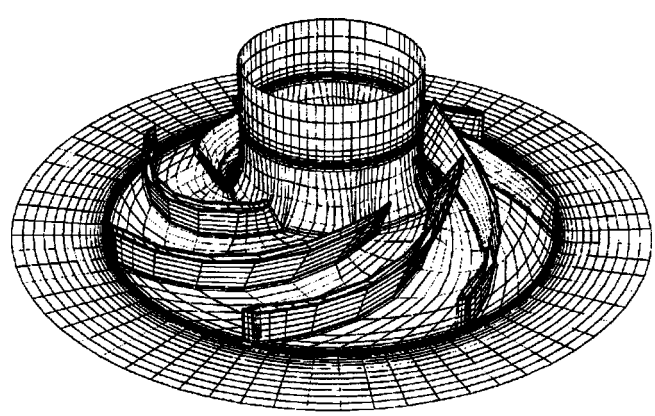

Fig. 8 360-deg seven-bladed impeller model

Table 1 Summary of computational grids

Grid Block	Coarse (C1)	Medium (Med)	Fine (F1)
Inlet	15×12×50	15×12×70	15×12×70
7 imp. blocks	22×15×10	22×15×10	22×15×10
Diffuser	28×13×50	28×13×70	34×13×70
Upper shroud	23×13×50	23×13×70	36×19×70
Lower shroud	38×13×50	38×13×70	56×17×70
Face seal	16×6×50	16×6×70	16×6×70
No. of nodes	94750	123410	187880
CPU time per PFR (min)	152	175	263

three models of reasonable in size for modern workstations. The CPU time listed is for an SGI MIPS 10000, 195 MHz processor. Notice that the CPU times varies linearly with model size, a favorable characteristic of the multigrid solver.

Description of Experimental Setup

Bolleter et al.[2] utilize a hydraulic exciter that inputs a swept sine into the system. Impeller forces are measured using a six-bridge strain gauge arrangement that is fed into a rotating amplifier and out of the rotor through slip rings. Impedance functions are determined using the measured response. Since vaned diffusers are used (with volute far down stream), symmetry of the force coefficients is assumed. Synchronous time averaging (STA) is employed to reduce the effect of forces not coherent with the rotor motion. The impedance functions are determined from the STA forces and displacements. A frequency range from 10–150 percent of running speed is used. Data is sampled at 32 points/rev for 32 revolutions, and 100 averages are used. Tests are performed at 2000 rpm with cold water (30°C) and is the data utilized in the present study. Other tests are performed at higher speeds (4000 rpm) and water temperatures up to 160°C. Table 2 gives impeller dimensions and characteristics.

Performance Predictions

While the total head rise (impeller+diffuser) was measured to be 68 meters, the head rise across the impeller is 48.25 m. Table 3 compares the predicted head with experiment.

The predicted head correlates well with experiment for all three grids. The experimental efficiency is a stage value including both the impeller and diffuser, while the prediction is just for the impeller. The average inlet swirl ratio (W_{rat}) at the entrance to the shroud (impeller tip) compares well to measured Pitot tube measurements and changes little after the medium grid.

Table 2 Sulzer Impeller Data

Geometry Information	Dimension
Impeller blade tip diameter	350 mm
Impeller shroud diameter	350.4 mm
Impeller discharge width	28 mm
Number of impeller blades	7
Rotation speed	2000 rpm
Design flow	130 l/s
n_q	33

Table 3 Sulzer performance data

Grid	Impeller Isentropic Head (m)	Isentropic Efficiency (%)	Avg. Tang. Swiri (Shroud Inlet)
Coarse grid	49.02	93.1	0.52
Medium grid	49.11	93.2	0.51
Fine grid	49.08	93.20	0.52
Experiment	48.25	84	~0.5

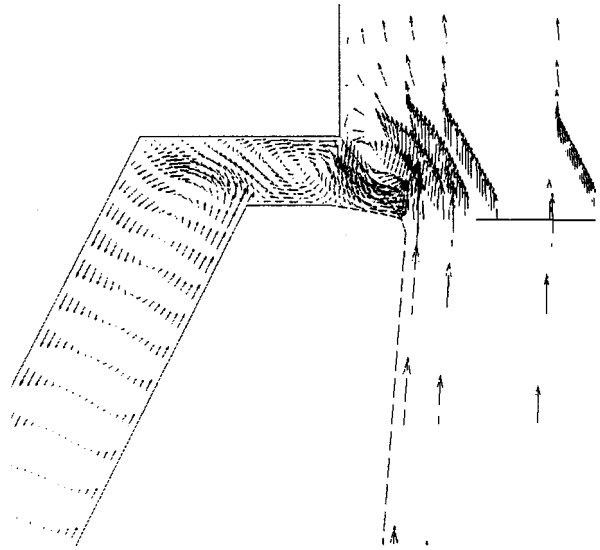

Fig. 9 Computed velocity vectors at impeller tip (F1 grid)

Figure 9 is a vector plot in the meridonal plane at the impeller tip and demonstrates the complex flow field at the shroud entrance, showing the presence of several recirculation zones. The viscous pumping action near the shroud wall causes reverse flow toward the tip, while pressure forces drive the flow downward near the stator wall. Figures 10 and 11 show several more recirculation zones near the "elbow" of the shroud and at the face seal entrance. The relative velocities from each domain are transformed into the absolute (fixed) frame of reference. Figure 12 plots the absolute tangential swirl contours. Notice that the swirl velocity is a maximum near the tip of the shroud and decreases while traveling down the shroud path (toward the seal). This decrease conflicts with free vortex principles (conservation of angular momentum), which predicts an increase in swirl velocity as the radius is decreased. Viscous effects from the stator wall cause this deceleration despite the shroud rotation promoting swirl. Clearly, any abstraction (i.e., inviscid or bulk-flow assumptions) that ignores the viscous effects in the shroud will not capture the true physics of the flow field.

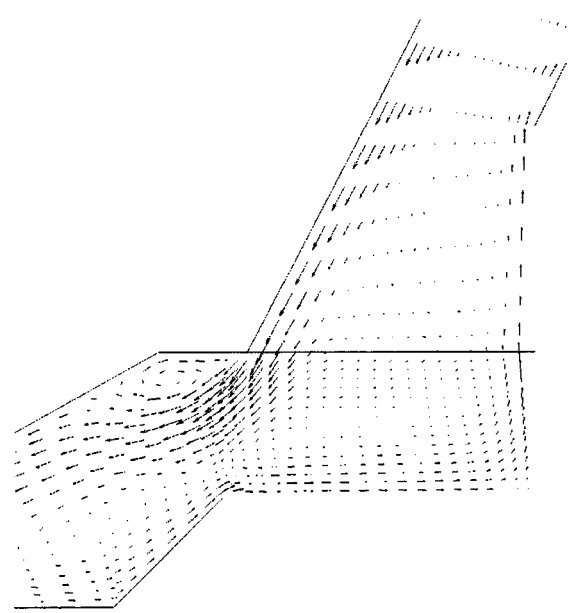

Fig. 10 Velocity vectors at shroud elbow (F1 grid)

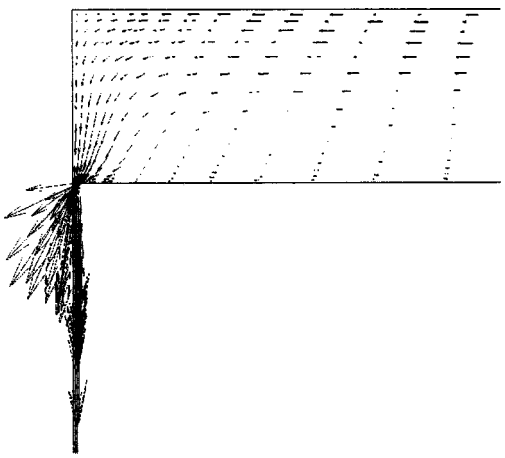

Fig. 11 Velocity vectors at seal entrance (F1 grid)

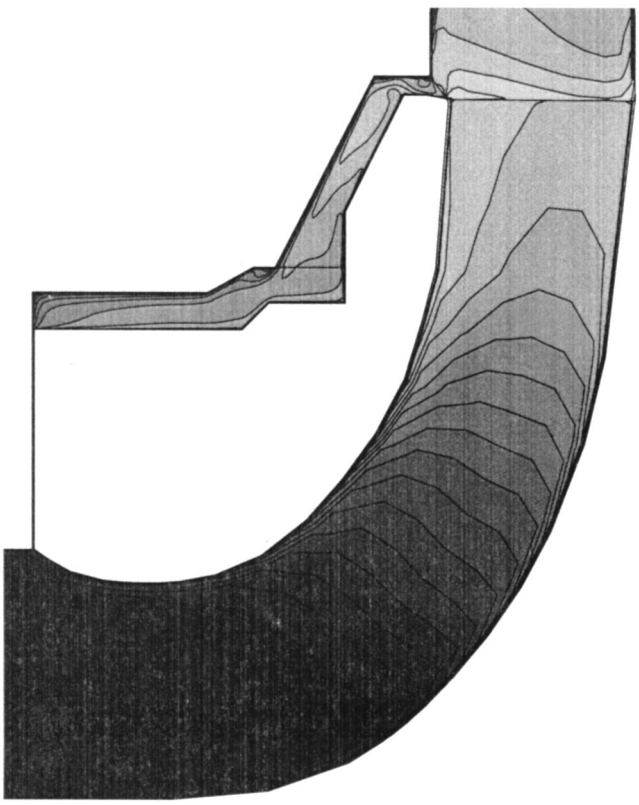

Fig. 12 Absolute tangential velocity contours (F1 grid)

Rotordynamic Prediction

To validate the pressure integration algorithm and to verify full convergence, a zero-eccentricity case was first run to confirm that the impedance forces are indeed zero. The shroud is then made eccentric and recalculated. The pressure distribution at the entrance to the impeller is plotted in Fig. 13 and shows the fundamental pressure field giving rise to the rotordynamic forces plus a higher frequency (7X) due to the wakes off the impeller blades. The predicted impedance force for the fine grid (F1) (at PFR values of 0, 0.25, 0.5, 0.75, 1.0, 1.5, and 2.0) along with the curve-fits for all three grids at are plotted in Fig. 14. Mesh independence is established for the medium grid density, which shows identical results with the fine grid. The plot shows reasonable Fr prediction at the lower frequencies but underpredicts the radial

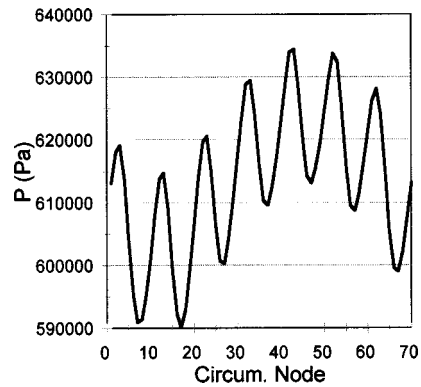

Fig. 13 Shroud inlet pressure distribution

impedance at higher PFR's, since the large inertial of the fluid inside the primary passage of the impeller is not considered. The tangential impedance shows good correlation at the subsynchronous precessional frequencies (PFR<1). These results are in agreement with the experimental investigation of Ohashi et al.[6] which demonstrated most of the direct and cross-coupled stiffness arises from the shroud passage. The predicted PFR at the neutral stability point (WFR$=0.62$) is identical with experiment. The rotordynamic coefficients resulting from these curve-fits are summarized in Table 4 and are compared to those of Baskharone et al.[14] and Childs [13].

The contribution of the impeller (due to eccentric shroud) is relative small but does further improve the predictions. The results show good stiffness prediction and slightly over predictions the

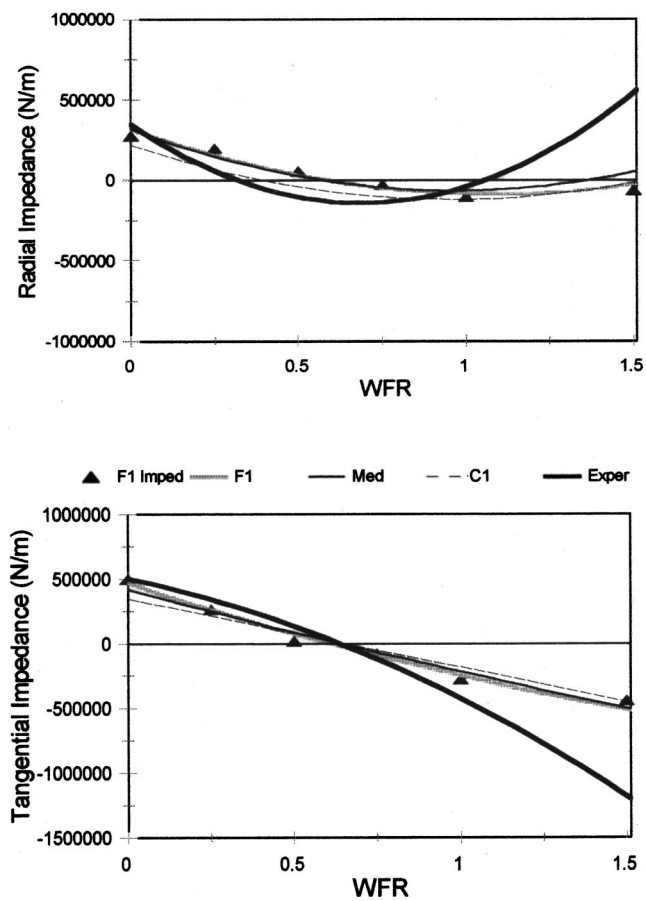

Fig. 14 Effect of grid density of impedance curves

Table 4 Summary of predicted rotordynamic force coefficients

Mesh/Components	K KN/m	k KN/m	c KN-c/m	c KN-c/m	M kg	m kg
Coarse grid (shroud only)	−180	370	2.80	3.04	8.11	−1.28
Coarse grid (shroud+imp)	−223	350	2.52	3.37	8.34	0.07
Med. grid (shroud only)	−286	448	3.59	3.62	9.30	−2.67
Med. grid (shroud+imp)	−323	420	3.26	3.79	9.32	−1.05
Fine grid (shroud only)	−284	501	4.40	3.35	7.77	−4.55
Fine grid (shroud+imp)	−324	471	4.05	3.59	7.92	−2.92
Experiment	−353	506	2.58	6.80	23.6	8.85
Experimental uncertainty	22	24	0.16	0.17	0.56	0.62
Baskharone et al. [14]	−268	165	1.64	2.92	5.03	3.03
Childs [13] ($W_{rat}\approx 0.5$)	−42	288	2.02	2.29	8.96	−0.009

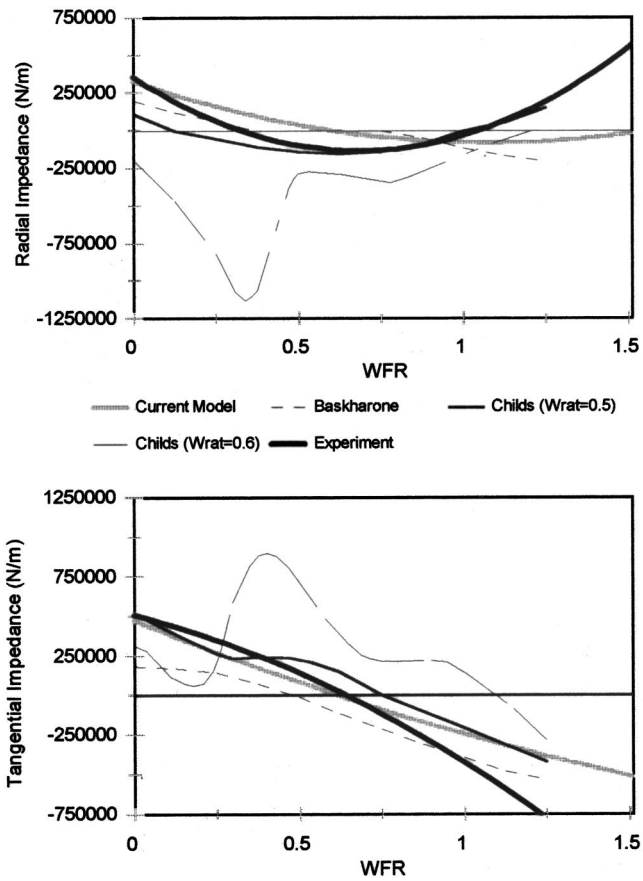

Fig. 15 Comparison of impedance curves

direct damping. The cross-coupled and inertial coefficients are under predicted since whirling forces from the impeller primary flow passage are not considered.

Figure 15 compares the F1 impedance curves with those of Baskharone and Childs. Overall, an improvement over these previous studies is realized especially at the lower precessional frequencies. The fluctuating curve represents the bulk-flow model with inlet swirl ratio (W_{rat}) equal to 0.6. These "resonances" previously described appear to be an anomaly unique to the bulk-flow model.

Summary and Conclusions

A commercial CFD code is adapted to solve for rotordynamic coefficients in a shrouded pump impeller. The code demonstrates close prediction of mean velocity profiles in the complex flow field of a grooved annular (labyrinth) seal. A finite whirl analysis is performed on a shrouded pump impeller by solving the coupled primary/secondary flow field at different precessional frequencies. Integration of the resulting pressure field in both the shroud and impeller regions yields the rotordynamic impedances. A curve-fit to a linear second-order model yields the rotordynamic force coefficients. The coupled model captures the complex flow field entering the shroud at the impeller tip, eliminating the need to specify these boundary conditions. Comparisons to the experimental results of a boiler feed pump impeller show good overall correlation especially in the subsynchronous regime, which is important for good rotordynamic stability assessment. The 360 deg model employed here may be easily generated from traditional "pie" models allowing a full concurrent design approach with the performance, structural, and rotordynamic analysis.

Acknowledgment

The authors would like to thank Marshall Space Flight Center for funding this research. Special thanks also goes to Mr. Arno Frei at Sulzer Brothers, Ltd., for providing additional details of the experimental impeller testing.

Nomenclature

A_x, A_y = Cartesian area components of cell face
E = surface roughness parameter = 9.0
F_n, F_t = normal (radial) and tang, reaction force (N)
$\bar{F}_n$, $\bar{F}_t$ = normal (radial) and tang, impedance (F/ϵ) (N/m)
H = pump head (ft or m)
K, C, M = direct stiffness, damping, mass (N/m, N-s/m, kg)
k, c, m = cross-coupled stiffness, damping, mass (N/m, N-s/m, kg)
N = speed (rpm)
Ns = $NQ^{1/2}/H^{3/4}$ = specific speed (using rpm, gpm, ft)
n_q = specific speed (using rpm, m^3/s, m)
P = local static pressure (Pa)
Q = flow (gpm or m^3/s)
R_2 = impeller tip radius (m)
Re = Reynolds number = $2\rho Uc/\mu$
S_{ij} = mean strain rate [1/s] = $1/2(\partial U_i/\partial x_j + \partial U_j/\partial x_i)$
u = velocity component tangent to wall (m/s)
u_i = fluctuation velocity component (m/s)
U_i = mean velocity component (m/s)
U_τ = shear velocity (m/s)
PFR = precessional frequency ratio = Ω/ω
WFR = PFR at the neutral stability point
y = distance from wall to first nodal point (m)
β_2 = exit blade angle (meas. from radial)
δ_{ij} = Kronecker delta
ϵ = eccentricity (m)
ε = turbulent kinetic energy dissipation (m^2/s^3)
κ = turbulent kinetic energy (m^2/s^2)
K = von Kármán constant = 0.4
μ = molecular viscosity (Pa-s)
μ_t = turbulent (eddy) viscosity (Pa-s)
τ_w = wall shear stress (Pa)
ω = rotation speed (rad/sec)
Ω = precessional speed (rad/sec) = PFR $\cdot\,\omega$

References

[1] Wachel, J. C., and von Nimitz, W. W., 1981, ''Ensuring the Reliability of Offshore Gas Compressor Systems,'' J. Pet. Technol., **33**, No. 11, pp. 2252–2260.

[2] Bolleter, U., Leibundgut, E., and Sturchler, R., 1989, ''Hydraulic Interaction and Excitation Forces of High Head Pump Impellers,'' *Pumping Machinery-1989*, Proceedings of the Third Joint ASCE/ASME Mechanics Conference, La Jolla, CA, NASA Science and Technical Branch, pp. 187–194.

[3] Jery, B., Acosta, A. J., Brennen, C. E., and Caughey, T. K., 1984, ''Hydrodynamic Impeller Stiffness, Damping, and Inertia in the Rotordynamics of Centrifugal Pumps,'' *Rotordynamic Instability Problems in High-Performance Turbomachinery*, NASA CP2338, proceedings of a workshop held at Texas A & M University, NASA Science and Technical Branch, pp. 137–160.

[4] Adkins, D. R., and Brennen, C. E., 1988, ''Analysis of Hydrodynamic Radial Forces on Centrifugal Pump Impellers,'' ASME J. Fluids Eng., **110**, No. 1, pp. 20–28.

[5] Uy, R. V., 1998, ''Studies of Rotordynamic Forces Generated by Annular Flows,'' Ph.D. dissertation, California Institute of Technology, Mechanical Engineering Department.

[6] Ohashi, H., Sakurai, A., and Nishihama, J., 1988, ''Influence of Impeller and Diffuser Geometries on the Lateral Fluid Forces of Whirling Centrifugal Impeller,'' *Rotordynamic Instability Problems in High-Performance Turbomachinery*, NASA CP3026, proceedings of a workshop held at Texas A&M University, NASA Science and Technical Branch, pp. 285–306.

[7] Bolleter, U., Wyss, A., Welte, L., and Strchler, R., 1987, ''Measurement of Hydrodynamic Interaction Matrices of Boiler Feed Pump Impellers,'' ASME J. Vibr. Acoust., **109**, pp. 144–151.

[8] Guinzburg, A., 1992, ''Rotordynamic Forces Generated By Discharge-to-Suction Leakage Flows in Centrifugal Pumps,'' Ph.D. dissertation, California Institute of Technology, Mechanical Engineering Department.

[9] Sivo, J. M., Acosta, A. J., Brennen, C. E., and Caughey, T. K., 1995, ''The Influence of Swirl Brakes on the Rotordynamic Forces Generated by Discharge-to-Suction Leakage Flows in Centrifugal Pumps,'' ASME J. Fluids Eng., **117**, pp. 104–108.

[10] Colding-Jorgensen, J., 1980, ''Effect of Fluid Forces on Rotor Stability of Centrifugal Compressors and Pumps,'' in *Rotordynamic Instability in High Performance Turbomachinery*, Texas A & M University.

[11] Fongang, R., Colding-Jǿrgensen, J., and Nordmann, R., 1996, ''Investigation of Hydrodynamic Forces on Rotating and Whirling Centrifugal Pump Impellers,'' presented at the International Gas Turbine and Aeroengine Congress & Exhibition, Birmingham, UK, June 1–13.

[12] Torbergsen, E., and White, M. F., 1998, ''Numerical and Experimental Study of Impeller/Diffuser Interactions in Centrifugal Pumps,'' *Proceedings of the ISROMAC Conference*, Vol. C, Honolulu, HI, Feb. 22–26, Bird Rock Publishing House, pp. 1349–1358.

[13] Childs, D., 1989, ''Fluid-Structure Interaction Forces at Pump Impeller-Shroud Surfaces for Rotordynamic Calculations,'' Trans. ASME, **111**, pp. 216–223.

[14] Baskharone, E. A., Daniel, A. S., and Hensel, S. J., 1994, ''Rotordynamic Effects of the Shroud-to-Housing Leakage Flow in Centrifugal Pumps,'' ASME J. Fluids Eng., **116**, pp. 558–563.

[15] Wyman, N. J., 1994, ''Effects of the Primary Passage on the Flow Through the Secondary Passage of a Shrouded-Impeller Pump,'' Master's thesis, Mechanical Engineering Department, Texas A & M University.

[16] Dietzen, F. J., and Nordmann, R., 1987, ''Calculating Rotordynamic Coefficients of Seals by Finite Difference Techniques,'' ASME J. Tribol., **109**, pp. 388–394.

[17] Rhode, D. L., Hensel, S. J., and Guidry, M. J., 1992, ''Three-Dimensional Computations of Rotordynamic Force Distribution in a Labyrinth Seal,'' Tribol. Trans., **36**, No. 3, pp. 461–469.

[18] Arghir, M., and Frene, J., 1997, ''Rotordynamic Coefficients of Circumferentially-Grooved Liquid Seals Using the Average Navier-Stokes Equations,'' ASME J. Tribol., **119**, pp. 556–567.

[19] Athavale, M. M., Przekwas, A. J., Hendricks, R. C., and Liang, A., 1994, ''SCISEAL: A three-dimensional CFD Code for Accurate Analysis of Fluid Flow and Forces in Seals,'' Advance ETO Propulsion Conference, May.

[20] Moore, J. J., and Palazzolo, A. B., 1998, ''CFD Comparison to Three-Dimensional Laser Anemometer and Rotordynamic Force Measurements for Grooved Liquid Annular Seals,'' presented at the ASME/STLE International Tribology Conference, Oct. 25–29, Toronto, Ontario, Canada.

[21] AEA, 1997, TASCflow Documentation Ver. 2.7, AEA Technologies, Waterloo, Ontario, Canada.

[22] Raw, M., 1996, ''Robustness of Coupled Algebraic Multigrid for the Navier-Stokes Equations,'' AIAA paper.

[23] Morrison, G. L., Johnson, M. C., and Tatterson, G. B., 1991, ''three-dimensional Laser Anemometer Measurements in a Labyrinth Seal,'' ASME J. Eng. Gas Turbines Power, **113**, No. 1, pp. 119–125.

[24] Bhattacharya, A., 1997, ''CFD Based Rotordynamic Coefficients for Labyrinth Seals and Impeller Shroud Leakage Paths,'' Master's thesis, Mechanical Engineering Department, Texas A & M University.